10-2-2009

Preferential Growth of Single-Walled Carbon Nanotubes with Metallic Conductivity

Avetik R. Harutyunyan
Honda Res Inst

Gugang Chen
Honda Res Inst

Tereza M. Paronyan
University of Louisville

Elena M. Pigos
Honda Res Inst

Oleg A. Kuznetsov
Honda Res Inst

See next page for additional authors

Authors
Avetik R. Harutyunyan, Gugang Chen, Tereza M. Paronyan, Elena M. Pigos, Oleg A. Kuznetsov, Kapila Hewaparakrama, Seung M. Kim, Dmitri Zakharov, E A. Stach, and Gamini U. Sumanasekera

We have thus demonstrated that an array of Josephson junctions with appropriately chosen parameters can perform two functions simultaneously: short-circuit the offset charge variations of a small junction and protect the strong nonlinearity of its Josephson inductance from quantum fluctuations. The data show that the array possesses a microwave inductance 10^4 times larger than the geometric inductance of a wire of the same length (20 μm). The reactance of such an inductor is about 20 $R_Q \approx 20$ kΩ at 10 GHz, whereas its resistance is less than 1 Ω. The spectrum of the fluxonium qubit suggests that it is as anharmonic as the flux qubit but as insensitive to flux variations as the transmon qubit. Possible applications of this single Cooper-pair charging effect immune to charge noise include the observation of fully developed macroscopic quantum-coherent oscillations between fluxon states (*25*), the search for Λ or V transition configurations for the shelving of quantum information (*26*) in superconducting artificial atoms, topological protection of superconducting qubits (*27*), and, finally, the long-sought quantum metrology of electrical current via Bloch oscillations (*28*, *29*).

References and Notes

1. H. Grabert, M. H. Devoret, Eds., *Single Charge Tunneling: Coulomb Blockade Phenomena in Nanostructures* (Plenum, New York, 1992).
2. B. D. Josephson, *Rev. Mod. Phys.* **36**, 216 (1964).
3. V. Bouchiat, D. Vion, P. Joyez, D. Esteve, M. H. Devoret, *Phys. Scr.* **T76**, 165 (1998).
4. Y. Nakamura, Yu. A. Pashkin, J. S. Tsai, *Nature* **398**, 786 (1999).
5. D. Vion *et al.*, *Science* **296**, 886 (2002).
6. K. Bladh, T. Duty, D. Gunnarsson, P. Delsing, *N. J. Phys.* **7**, 180 (2005).
7. M. Metcalfe *et al.*, *Phys. Rev. B* **76**, 174516 (2007).
8. J. M. Martinis, S. Nam, J. Aumentado, C. Urbina, *Phys. Rev. Lett.* **89**, 117901 (2002).
9. I. Chiorescu, Y. Nakamura, C. J. P. M. Harmans, J. E. Mooij, *Science* **299**, 1869 (2003).
10. J. A. Schreier *et al.*, *Phys. Rev. B* **77**, 180502(R) (2008).
11. R. P. Feynman, R. B. Leighton, M. Sands, *The Feynman Lectures on Physics* (Addison-Wesley, Reading, MA, 1964), vol. 2, chap. 23.
12. The ratio $(\mu_0/\varepsilon_0)^{1/2}/R_Q = 16\pi\alpha$, where $\alpha \approx 1/137$ is the fine structure constant.
13. J. Koch *et al.*, *Phys. Rev. A* **76**, 042319 (2007).
14. K. A. Matveev, A. I. Larkin, L. I. Glazman, *Phys. Rev. Lett.* **89**, 096802 (2002).
15. Materials and methods are available as supporting material on *Science* Online.
16. Because of coupling of the fluxonium circuit to the readout resonator (Fig. 1D), C_J is renormalized to the value $C_J + C_c$, with corrections on the order of $C_c/C_R \cong 1\%$.
17. Here we acknowledge experiments (*30*, *31*) in which a small Josephson junction was dc-biased in series with a micrometer-scale disordered film resistance exceeding R_K (*30*) or with an array of small-junction superconducting quantum interference devices (SQUIDs) (*31*) with zero-bias resistance tuned by magnetic field to exceed R_K. Both experiments aimed at protecting the small junction from the shunting effect of a low-impedance environment, using highly dissipative biasing elements. Although the results of dc current-voltage measurements were consistent with single Cooper-pair effects, they were distorted by Joule heating and other out-of-equilibrium effects in these biasing elements. We avoid the problem of dissipation with an array employing the pure Josephson kinetic inductance.
18. A. Wallraff *et al.*, *Nature* **431**, 162 (2004).
19. M. Devoret, in *Quantum Fluctuations in Electrical Circuits*, S. Reynaud, E. Giacobiano, J. Zinn-Justin, Eds. (Elsevier Science, Amsterdam, 1997).
20. J. Koch, V. Manucharyan, L. Glazman, M. Devoret, available at http://arxiv.org/abs/0902.2980 (2009).
21. Although the circuit in Fig. 1D might appear identical to the radio frequency (RF)–SQUID circuit (*32*), there is a drastic difference between the two when charging, Josephson, and inductive energies are compared. In addition, RF-SQUID is addressed by coupling to its flux degree of freedom via mutual inductance, whereas the fluxonium is addressed by coupling to its charge degree of freedom via capacitance C_c.
22. J. Raimond, M. Brune, S. Haroche, *Rev. Mod. Phys.* **73**, 565 (2001).
23. D. I. Schuster *et al.*, *Phys. Rev. Lett.* **94**, 123602 (2005).
24. A. Abragam, *The Principles of Nuclear Magnetism* (Oxford Univ. Press, Oxford, 1961).
25. A. J. Leggett, *J. Phys. Condens. Matter* **14**, R415 (2002) and references therein.
26. W. Nagourney, J. Sandberg, H. Dehmelt, *Phys. Rev. Lett.* **56**, 2797 (1986).
27. A. Kitaev, available at http://arxiv.org/abs/condmat/0609441 (2006).
28. D. V. Averin, A. B. Zorin, K. K. Likharev, *Zh. Exp. Teor. Phys.* **88**, 692 (1985).
29. K. K. Likharev, A. B. Zorin, *J. Low Temp. Phys.* **59**, 347 (1985).
30. L. S. Kuzmin, D. B. Haviland, *Phys. Rev. Lett.* **67**, 2890 (1991).
31. M. Watanabe, D. B. Haviland, *Phys. Rev. Lett.* **86**, 5120 (2001).
32. J. R. Friedman, V. Patel, W. Chen, S. K. Tolpygo, J. E. Lukens, *Nature* **406**, 43 (2000).

33. We acknowledge discussions with M. Brink, E. Boaknin, M. Metcalfe, R. Vijay, D. Schuster, L. DiCarlo, L. Frunzio, R. Schoelkopf, and S. Girvin. This research was supported by NSF under grants DMR-0754613 and DMR-032-5580, the National Security Agency through ARO grant no. W911NF-05-01-0365, the Keck Foundation, and the Agence Nationale pour la Recherche under grant ANR07-CEXC-003. M.H.D. acknowledges partial support from the College de France.

Supporting Online Material
www.sciencemag.org/cgi/content/full/326/5949/113/DC1
Materials and Methods
SOM Text
Fig. S1
Table S1
References

29 April 2009; accepted 28 July 2009
10.1126/science.1175552

Preferential Growth of Single-Walled Carbon Nanotubes with Metallic Conductivity

Avetik R. Harutyunyan,[1]* Gugang Chen,[1] Tereza M. Paronyan,[2] Elena M. Pigos,[1] Oleg A. Kuznetsov,[1] Kapila Hewaparakrama,[2] Seung Min Kim,[3,4] Dmitri Zakharov,[4] Eric A. Stach,[3,4] Gamini U. Sumanasekera[2]

Single-walled carbon nanotubes can be classified as either metallic or semiconducting, depending on their conductivity, which is determined by their chirality. Existing synthesis methods cannot controllably grow nanotubes with a specific type of conductivity. By varying the noble gas ambient during thermal annealing of the catalyst, and in combination with oxidative and reductive species, we altered the fraction of tubes with metallic conductivity from one-third of the population to a maximum of 91%. In situ transmission electron microscopy studies reveal that this variation leads to differences in both morphology and coarsening behavior of the nanoparticles that we used to nucleate nanotubes. These catalyst rearrangements demonstrate that there are correlations between catalyst morphology and resulting nanotube electronic structure and indicate that chiral-selective growth may be possible.

Carbon nanotubes have yet to see ubiquitous application in electronic devices, despite their electronic properties (*1*). This is largely because the electronic properties are related to nanotube bonding configuration (known as its chirality). Though some methods exist to bias the population of one type of nanotube during synthesis, there is only a limited understanding of exactly what determines chirality during synthesis.

There have been important achievements in separating single-walled carbon nanotubes (SWNTs) according to their conductivity (*2*–*5*) and in enriching the distribution of nanotubes with a specific conductivity (*6*, *7*). Meanwhile, there have been a few reports regarding direct control over nanotube structure during growth (*8*–*10*). The fact that SWNTs with narrow chiral distributions have been successfully grown (*8*) indicates that there may be a specific mechanism that controls chirality. The concept of amplifying existing SWNT distributions by seeding growth from another nanotube with well-defined chirality has been proposed (*9*); however, evidence for the maintenance of chirality has not yet been reported (*10*). The preferential growth of nearly 90 (*11*) to 96% (*12*) of semiconducting SWNTs by plasma-enhanced chemical vapor deposition has been reported, but the mechanism that leads to this selectivity remains unclear.

In this work, we grew SWNTs from Fe nanocatalysts deposited onto a SiO_2/Si support

[1]Honda Research Institute USA, 1381 Kinnear Road, Columbus, OH 43212, USA. [2]Department of Physics and Astronomy, University of Louisville, Louisville, KY 40292, USA. [3]School of Materials Engineering, Purdue University, 701 Northwestern Avenue, West Lafayette, IN 47907, USA. [4]Birck Nanotechnology Center, Purdue University, 1205 West State Street, West Lafayette, IN 47907, USA.

*To whom correspondence should be addressed. E-mail: aharutyunyan@honda-ri.com

and in situ annealed in a He or Ar ambient that contains various ratios of H_2 and H_2O. We used methane as the carbon source at 860°C (*13*). Scanning electron microscopy studies show that increasing concentration of reductive species during catalyst conditioning from Ar:H_2 (9:1) to Ar:H_2 (8:2) at 840 torr in the presence of ~3.5 mtorr of H_2O results in a relatively higher density of SWNTs on the substrate (fig. S1, A and B). In contrast, in the presence of a He-supported ambient with ~3.5 mtorr of H_2O, the density of grown SWNTs is high and does not show strong dependence on H_2 concentration (fig. S1, C and D). Raman spectroscopy analyses of these samples reveal that the ratio of metallic tubes to semiconducting tubes is sensitive to catalyst conditioning history.

The strong variations of nanotube density in different environments led us to perform systematic studies of SWNTs grown on catalysts that were in situ annealed under different ambients. For a reasonable estimation of the ratio of metallic tubes to semiconducting tubes, we used the integral intensities of the Raman radial breathing modes (RBMs), which we define as $R = I_{met.}/I_{sem}$ (here, I_{met} is the intensity of the metallic tubes, and I_{sem} is the intensity of the semiconducting tubes) (*2*). We used three excitation wavelengths (λ = 785, 632.8, and 532 nm) in our experiment. Of these, λ = 632.8

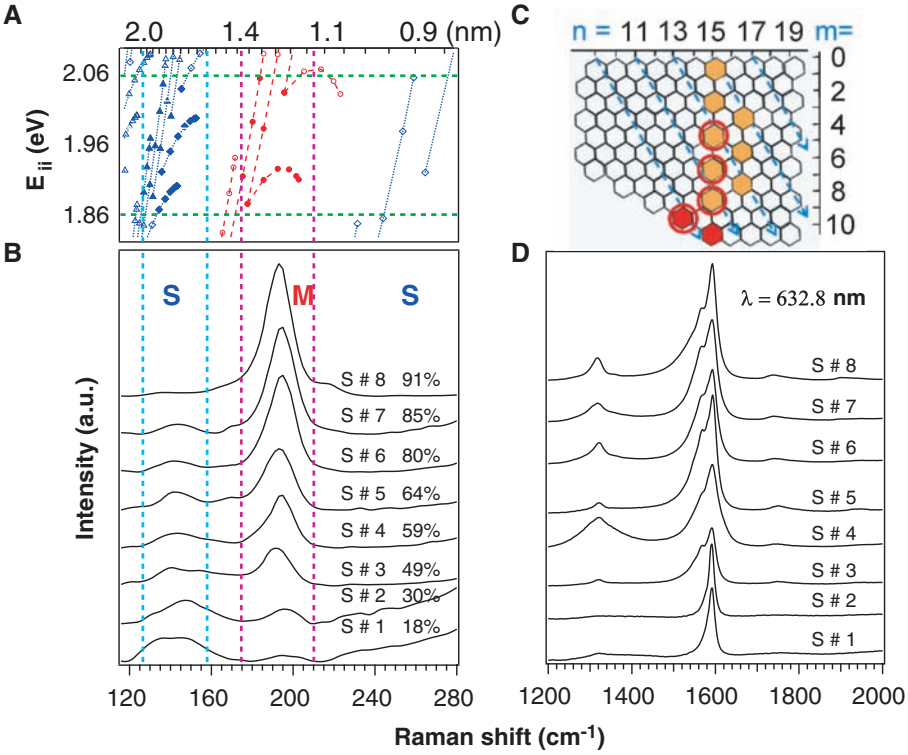

Fig. 1. The Raman spectra (λ = 632.8-nm laser wavelength) of SWNTs grown from preliminarily annealed Fe catalysts under different conditions. (**A**) Populations of the tubes whose optical transition energies E_{ii} are under resonance with laser excitation = 1.96 ± 0.1 eV (solid blue symbols, semiconducting tubes; solid red dots, metallic tubes). (**B**) Evolution of RBMs for semiconducting and metallic SWNTs, depending on the annealing ambient and duration. The estimated percentage of metallic tubes in each sample is shown. a.u., arbitrary units. (**C**) Chiral indices (*n*, *m*) assignments of the metallic tubes (open red circles, the tubes' chiralities that are matching closely with observed RBM peaks; red solid hexagons, metallic tubes; yellow solid hexagons, semimetallic tubes). (**D**) Evolution of G-band of corresponding SWNTs samples.

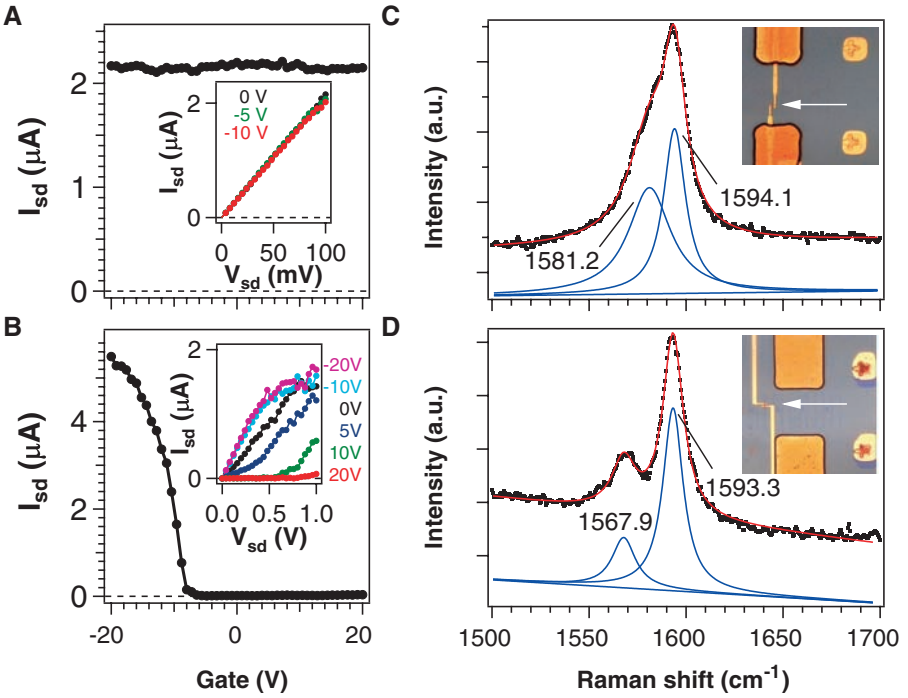

Fig. 2. Simultaneous electrical and Raman measurements (λ = 532-nm laser wavelength) of individual SWNTs. Typical electrical behavior for SWNTs incorporated in the FET device assigned as (**A**) metallic and (**B**) semiconducting. (Insets) *I-V* characteristics. V_{sd}, source-drain voltage. Corresponding Raman G-band spectrum for (**C**) metallic and (**D**) semiconducting SWNTs. The Lorentzian fittings are shown. (Insets) Optical images of the corresponding devices. The arrows indicate the locations of SWNTs.

nm resonates with roughly equal populations of both metallic and semiconducting tubes for the diameter range of the tubes grown in this study (~0.9 to 1.85 nm). Thus, our experiment can provide a reasonably accurate determination of the ratio of metallic tubes to semiconducting tubes (Fig. 1A) (*14*, *15*).

To obtain each spectrum, we averaged 50 individual Raman spectra, measured from different spots of the nanotube sample (the laser beam has a diameter of ~1 μm at the sample, and the distance between spots is ~10 μm). We observed two distinguishable regions in the RBM spectrum: (i) one in the range from 120 to 160 cm^{-1}, which is assigned to semiconducting tubes (S_{33}), and (ii) another band in the range from 160 to 230 cm^{-1}, which is assigned to metallic tubes (M_{11}). Figure 1B (S#1 and S#2) shows the Raman RBM spectra of the SWNTs grown on the Fe catalyst annealed under Ar:H_2 (9:1) and He:H_2 (9:1) for 5 min at 860°C in the presence of ~3.5 mtorr H_2O. The replacement of Ar with He leads to an increase in R from 0.34 to 0.77. Furthermore, with increasing H_2 content (Ar:H_2 at 8:2), the intensity of the RBM peaks originating from the semiconducting tubes declines, whereas the intensity for the RBM of the metallic tubes increases. This results in a variation of the corresponding RBM integral intensity ratio from $R = 0.34$ to 1.71 (S#1 and S#3), with a maximum of $R = 2.64$ in the case of the He:H_2 (8:2) ambient (S#4).

Next, to obtain the highest possible value of R, we performed parametrical studies of R for both He- and Ar-supported environments in the presence of ~3.5 mtorr H_2O and for different catalyst annealing durations at 860°C (from <1 min to a maximum of 10 min, S#5 to S#8). We achieved an R value of 3.22 for SWNTs grown from Fe particles annealed in an Ar:H_2 (8:2) ambient for 2 min and a dramatically high R value of 20.2 for He:H_2 (8:2) conditioning ambient for a 1 min annealing duration (S#5 and S#8, respectively). It is straightforward to conclude that for sample S#1, the RBM band of the as-grown tubes is dominated by semiconducting tubes ($R = 0.34$, S#1), whereas in the case of sample S#8, the dominant contribution corresponds to metallic tubes ($R = 20.2$). The G-band spectra (Fig. 1D) display transitions from Lorenzian to Breit-Wigner-Fano line shapes for the corresponding sequence of the samples (*13*) (fig. S2), and this supports these conductivity assignments (Fig. 1C) (*16*).

To obtain a reasonable quantitative estimation of the percentage of metallic tubes, we compared the integrated RBM peaks of the Raman spectra with the spectra of a reference sample (*2*, *11*, *12*). The use of commercially available high-pressure CO conversion (HiPco) SWNTs as the reference sample [we estimated a 37:63 ratio of metallic tubes to semiconducting tubes on the basis of photoluminescence measurements; see table S1, which contains a value close to that reported in (*11*) at a 39:61 ratio] results in a determination of a ~96% metallic tube fraction in the sample with the highest value of R (20.2, S#8). However, HiPco SWNTs show a noticeably different diameter distribution than do our samples, which may cause a large inaccuracy in this estimation, as the optical transitions are sensitive to the tube diameter. Therefore, we prepared reference samples of well-dispersed individual tubes grown on the same silicon substrate under analogous conditions as sample S#1 with $R = 0.34$ (Ar-supported ambient) (Fig. 1B). The substrate had special marks for identification of each tube by atomic force microscopy (AFM) (*13*) (fig. S3). We used eight laser excitation wavelengths (488, 514, 532, 570, 582, 610, 647, and 675 nm) for assignment of the tube's conductivity, and we made sure that each laser spot interrogated only one tube. We assigned a total of 80 different tubes as metallic or semiconducting based on the approach of previous theoretical and experimental studies (*17*, *18*). Among this population, five tubes could not be assigned. We found that the percentage of metallic tubes in this sample was 18% (± 3%).

To independently verify these Raman spectra analyses, we also performed transport measurements. The assignment of each individual nanotube was based on field-effect transistor (FET) performance (fig. S4, A and B). Overall, 32 FET devices were prepared and characterized according to their source-drain current (I_{sd}) versus gate voltage (V_g) behavior (Fig. 2, A and B). The statistics of the metallic-versus-semiconducting assignment process (*19*) are presented in Fig. 3A and show that 25% (± 5%) of the tubes were metallic nanotubes, and the other 75% were semiconducting nanotubes (two tubes were indeterminate), which is in reasonable agreement with the assignments based on Raman spectra results. Figure 2 shows an example of simultaneous electrical (Fig. 2, A and B) and Raman (Fig. 2, C and D) characterizations of the same tube, where the Raman profile also correlates with the electrical performance. Similar studies performed on the individual SWNTs grown on the catalysts annealed under He-supported ambient (~3.5 mtorr of H_2O), analogous to the conditions of sample S#4 with $R = 2.64$, show ~50% metallic tubes according to Raman assignments (a total of 119 tubes were assigned) and ~57% (± 5%) based on FET performance (72 FET devices were used for electrical characterizations) (Fig. 3B). These results confirm that the catalyst conditioning ambient affects the relative abundance of metallic and semiconducting tubes.

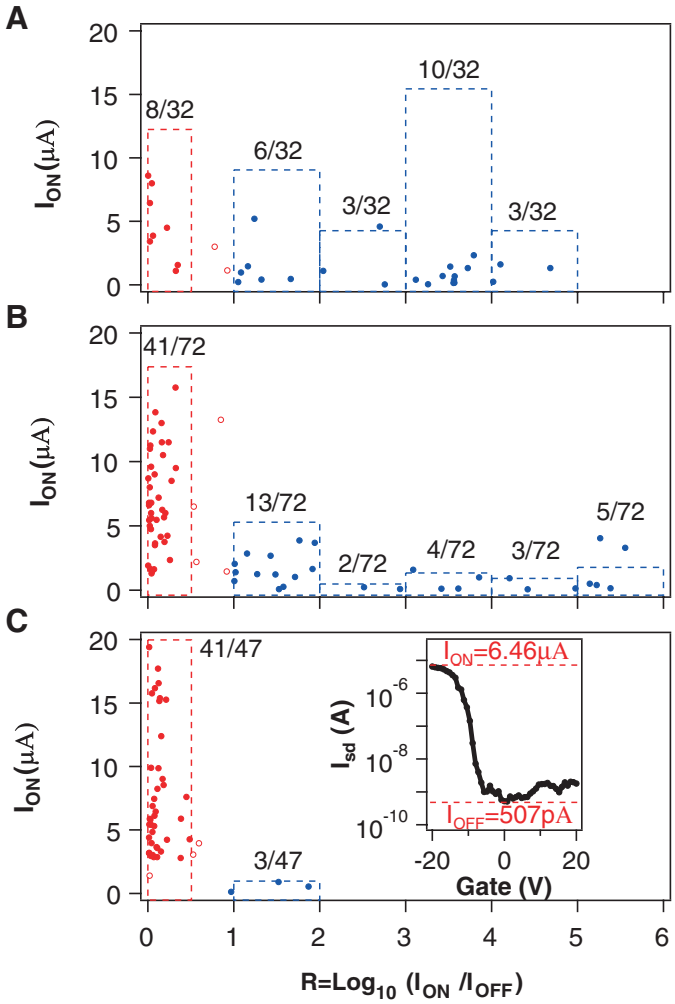

Fig. 3. Individual carbon nanotube FET device characterizations and histograms of assigned tubes for samples based on (**A**) S#1, (**B**) S#4, and (**C**) S#8. Red dots, metallic behavior; blue dots, semiconducting behavior (circles are not assigned). The inset in (C) shows the notation used for the electrical characteristics. I_{ON} is the on-state current, whereas I_{off} is the off-state current.

By using the prepared reference sample, we estimated the variation of the metallic tube contribution in the samples from ~18 up to ~91% (Fig. 1, from S#1 to S#8), depending on the ambient used for catalyst conditioning based on Raman spectra. To verify the accuracy of these estimations, independent quantification of the fraction of semiconducting nanotubes was made by comparing the number densities of SWNTs in images from near-infrared photoluminescence (which samples semiconducting species) and AFM (which samples all species) (*13*). This study indicated the presence of 15% (2.6% SE) semiconducting nanotubes and thus 85% metallic nanotubes for the sample S#6. This is in reasonable agreement with the Raman determinations (20 and 80%, respectively) (*13*). Moreover, for the sample with the highest estimated metallic content (91%), we performed electrical measurements as well (47 individual tube-based FET devices). These measurements indicated that 87% (± 6%) of the nanotubes were metallic (Fig. 3C), thereby supporting the estimated values. Although there were a few samples with percentages of metallic tubes in the range of 87 to 91%, SWNTs with a metallic tube concentration in the range of ~70 to 85% have been grown repeatedly.

To distinguish the effect of H_2 and H_2O species on the metallic-to-semiconducting ratio of the as-grown tubes, we performed a series of experiments using catalyst particles that were in situ annealed in only reductive (H_2) ambient supported by Ar or He without the presence of H_2O ($<7.6 \times 10^{-4}$ mtorr). In these cases, we did not observe any difference between the use of Ar- or He-supported ambient (fig. S5). Thus, the presence of H_2 alone in the ambient does not lead to the preferential growth of metallic tubes. One can therefore conclude that it is the presence of H_2O in the catalyst annealing ambient supported by He that promotes the growth of metallic tubes, whereas the same amount of H_2O supported by Ar ambient is more favorable for semiconducting tubes. These facts also rule out the possibility of in situ modification of the electronic structure of the tubes via chemisorption of ambient species (*13*, *20*).

To gain insight into the mechanism by which the catalyst conditioning could alter the ratio of metallic tubes–to–semiconducting tubes, we performed in situ transmission electron microscopy (TEM) observations of the SiO_2-supported Fe nanocatalysts in H_2O, H_2/H_2O, Ar/H_2O, and He/H_2O gaseous environments under pressures of H_2O ~10^{-2} and 500 mtorr for H_2, He, and Ar, respectively. We used the same catalyst preparation procedure as for the ex situ growth of nanotubes (*13*). Before TEM measurements, we carried out in situ reduction of the particles by exposing them to hydrogen gas at 500°C at a pressure of 500 mtorr for 3 hours. The TEM images reveal a strong difference in the ripening behavior of Fe nanoparticles depending on the gas environment at 500°C (Fig. 4, A to C). Under H_2/H_2O ambient, we observed a negligible change in particle size, even after 90-min exposure. However, after 60 min in He/H_2O ambient, there is a small but noticeable increase in the particles' size, whereas a dramatic ripening is observed after only 15 min of annealing in the Ar/H_2O environment. This ripening behavior under Ar/H_2O is notable and becomes even more severe as the Ar gas pressure increases up to ~1.3 torr (fig. S6). Remarkably, high-resolution images taken at 500°C upon introducing He/H_2O and Ar/H_2O gas reveal that the particles also undergo reversible shape changes (Fig. 4). In the presence of a He/H_2O ambient (Fig. 4D), the particle is very faceted, with sharp corners, similar to our observations in H_2/H_2O ambient. In contrast, upon switching to Ar/H_2O ambient, the particle becomes more rounded (Fig. 4E). Upon returning to He/H_2O,

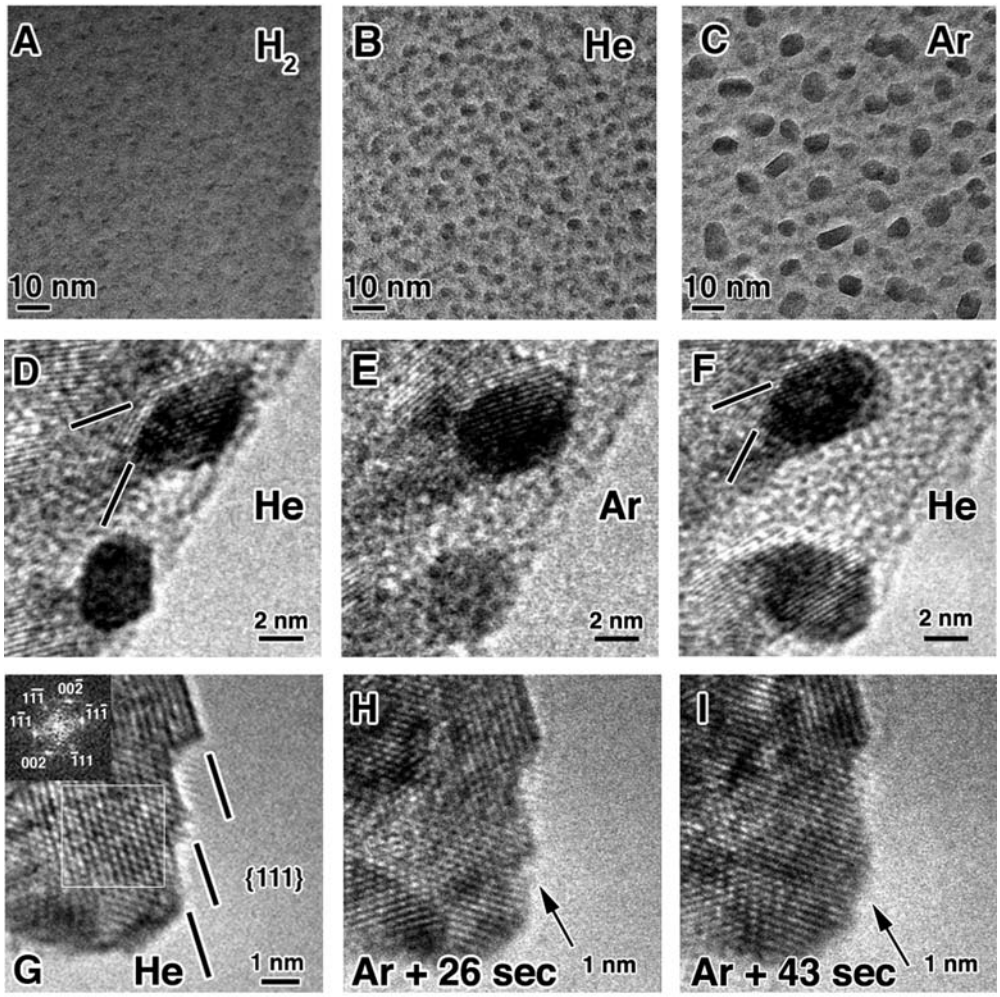

Fig. 4. High-resolution transmission electron micrographs of Fe catalyst as a function of gas environment. (**A** to **C**) Size evolution of Fe catalysts after 60 min under H_2 (A), He (B), and Ar (C) at 500°C and 500 mtorr. (**D** to **F**) Series of images from the same two Fe catalyst particles held at 500°C, as the gas overpressure is changed from (D) 500 mtorr He to (E) 500 mtorr Ar to (F) 500 mtorr He. (**G** to **I**) Series of images from a larger Fe catalyst particle along a 110 zone axis. (G) Image taken in 500 mtorr He at 500°C, showing very strong {111} facets. The inset diffractogram confirms the zone axis orientation. (H) After the introduction of Ar, local degradation of the facets begins. (I) With further time at 500°C in the Ar environment, the facet has been completely removed. For all cases, the H_2O with base pressure of 10^{-2} mtorr is present. Arrows in (H) and (I) indicate the gradual defaceting features over time.

the same strong faceting is yet again observed (Fig. 4F) (movie S1). This behavior was found to be ubiquitous, with all particles in He showing stronger faceting, and those in Ar exhibiting a more rounded shape.

We also investigated relatively larger catalyst sizes to more clearly observe the evolution of catalyst shapes. Figure 4G indicates that the equilibrium shape of the catalyst in the 500°C and 500 mtorr of He/H_2O environment has {111} facets with very sharp edges, which is exactly the same observation as in Fig. 4D. Figure 4, H and I, (movie S2) tracks the gradual defaceting of the hill-and-valley structure with increasing time at the same temperature after the removal of He/H_2O and the addition of Ar/H_2O. All of the observations reflected in Fig. 4 are consistent: Catalysts in the He/H_2O environment are strongly faceted. Additionally, the fact that the particles are more faceted in H_2/H_2O and He/H_2O ambients is consistent with the observation of a reduced ripening rate.

Broadly, the adsorbent-induced variation of the surface free energy $\Delta\gamma$ of the facets with Miller indices (h, k, l) on the particle can be expressed by

$$\Delta\gamma_{h,k,l} = \Delta\gamma_{h,k,l}(P, T, C_S, \theta_o, k_d, S) \qquad (1)$$

where P is the partial pressure of the adsorbate, T is the temperature, C_S is the surface concentration of the particle surface atoms, θ_o is the saturation coverage of the adsorbate, k_d is the desorption rate constant, and S is the sticking probability of the adsorbate (*21*, *22*). Our TEM data suggest that the surface energy anisotropy of specific facets of Fe is affected differently by the He/H_2O and Ar/H_2O ambients, resulting in the observed dynamic alterations in the particle shape. It is unlikely that the inert gas itself causes a difference in surface free energy via adsorption at high temperatures. Therefore, the entirety of our data set indicates that it is most probable that H_2O adsorption is responsible for the induced surface reconstruction (*23*). The adsorption pathway can be either dissociative (with formation of adsorbed hydroxyl, atomic oxygen, and atomic hydrogen species on the surface) or molecular (*24*). However, analysis of the catalyst structure (through the use of diffractograms produced by fast Fourier transforms of the images, shown as an inset to Fig. 4G, indicating that the particles are γ-Fe) and observation of reversible shape changes (Fig. 4, D to F) suggest that there is no strong oxygen binding, which could have an impact on tube growth (*25*, *26*). The TEM measurements were performed under conditions of dynamic adsorption/desorption equilibrium with both H_2O and either He or Ar gas present. Both the observation of an adsorbent-induced reversible shape reconstruction and severe particle ripening under the Ar/H_2O environment (fig. S6) are consistent with the adatom's coverage of the Fe particles being greater in the He versus the Ar ambient [$\theta_{(He+H2O)} > \theta_{(Ar+H2O)}$]. This would also be correlated to the resulting, relatively low density of grown tubes under Ar-supported ambient (fig. S1). Thus, it appears that the addition of H_2O not only assists the super growth of nanotubes by etching the amorphous carbon (*27*) and controls the particle diameter by retarding the effect of Ostwald ripening (*28*), but also alters the shape of the particle. Remarkably, Yamada *et al.* (*29*) observed the alteration of carbon coated Fe catalysts into flatter particles upon the removal of the carbon coating by water treatment, under standard water-assisted nanotube growth conditions. There are other adsorbates (such as CO and O_2) that, in combination with the carbon source, may be even more effective at altering the catalyst size and morphology. Our results indicate that, with further optimization, direct control over nanotube structure during growth may well be feasible (*30*, *31*).

References and Notes

1. R. Saito, G. Dresselhaus, M. S. Dresselhaus, *Physical Properties of Carbon Nanotubes* (Imperial College Press, London, 1998).
2. R. Krupke, F. Hennrich, H. V. Löhneysen, M. M. Kappes, *Science* **301**, 344 (2003); published online 26 June 2003 (10.1126/science.1086534).
3. M. S. Strano *et al.*, *Science* **301**, 1519 (2003).
4. A. G. Rinzler, *Nat. Nanotechnol.* **1**, 17 (2006).
5. M. S. Arnold, A. A. Green, J. F. Hulvat, S. I. Stupp, M. C. Hersam, *Nat. Nanotechnol.* **1**, 60 (2006).
6. P. G. Collins, M. S. Arnold, P. Avouris, *Science* **292**, 706 (2001).
7. Y. Miyata, Y. Maniwa, H. Kataura, *J. Phys. Chem. B* **110**, 25 (2006).
8. S. M. Bachilo *et al.*, *J. Am. Chem. Soc.* **125**, 11186 (2003).
9. Y. Wang *et al.*, *Nano Lett.* **5**, 997 (2005).
10. R. E. Smalley *et al.*, *J. Am. Chem. Soc.* **128**, 15824 (2006).
11. Y. Li *et al.*, *Nano Lett.* **4**, 317 (2004).
12. L. Qu, F. Du, L. Dai, *Nano Lett.* **8**, 2682 (2008).
13. Material and methods are available as supporting material on *Science* Online.
14. H. Kataura *et al.*, *Synth. Met.* **103**, 2555 (1999).
15. M. Zheng *et al.*, *Science* **302**, 1545 (2003).
16. A. M. Rao, P. C. Eklund, S. Bandow, A. Thess, R. E. Smalley, *Nature* **388**, 257 (1997).
17. G. G. Samsonidze *et al.*, *Appl. Phys. Lett.* **85**, 5703 (2004).
18. J. Maultzsch, H. Telg, S. Reich, C. Thomsen, *Phys. Rev. B* **72**, 205438 (2005).
19. N. Izard *et al.*, *Appl. Phys. Lett.* **92**, 243112 (2008).
20. G. Zhang *et al.*, *J. Am. Chem. Soc.* **128**, 6026 (2006).
21. N. A. Gjostein, *Acta Metall.* **11**, 957 (1963).
22. G. Medeiros-Ribeiro, A. M. Bratkovski, T. I. Kamins, D. A. A. Ohlberg, R. S. Williams, *Science* **279**, 353 (1998).
23. P. L. Hansen *et al.*, *Science* **295**, 2053 (2002).
24. P. A. Theil, T. E. Madey, *Surf. Sci. Rep.* **7**, 211 (1987).
25. A. R. Harutyunyan, B. K. Pradhan, U. J. Kim, G. Chen, P. C. Eklund, *Nano Lett.* **2**, 525 (2002).
26. E. Mora, J. Pigos, F. Ding, B. I. Yakobson, A. R. Harutyunyan, *J. Am. Chem. Soc.* **130**, 11840 (2008).
27. K. Hata *et al.*, *Science* **306**, 1362 (2004).
28. P. B. Amama *et al.*, *Nano Lett.* **9**, 44 (2009).
29. T. Yamada *et al.*, *Nano Lett.* **8**, 4288 (2008).
30. R. H. Baughman, A. A. Zakhidov, W. A. de Heer, *Science* **297**, 787 (2002).
31. P. Avouris, *Acc. Chem. Res.* **35**, 1026 (2002).

32. We thank M. S. Dresselhaus and J. Kong for help in Raman measurements, B. Weisman and A. Naumov for photoluminescence measurements, B. I. Yakobson for discussions, and B. Maruyama for assistance. A patent related to this work has been submitted (U.S. patent application no. 12/511,047). This research was supported by the Honda Research Institute USA.

Supporting Online Material
www.sciencemag.org/cgi/content/full/326/5949/116/DC1
Materials and Methods
Figs. S1 to S6
Table S1
References
Movies S1 and S2

11 June 2009; accepted 6 August 2009
10.1126/science.1177599

Chiral Organic Ion Pair Catalysts Assembled Through a Hydrogen-Bonding Network

Daisuke Uraguchi, Yusuke Ueki, Takashi Ooi*

Research to develop structurally discrete, chiral supramolecular catalysts for asymmetric organic transformations has met with limited success. Here, we report that a chiral tetraaminophosphonium cation, two phenols, and a phenoxide anion appear to self-assemble into a catalytically active supramolecular architecture through intermolecular hydrogen bonding. The structure of the resulting molecular assembly was determined in the solid state by means of x-ray diffraction analysis. Furthermore, in solution the complex promotes a highly stereoselective conjugate addition of acyl anion equivalents to α,β-unsaturated ester surrogates with a broad substrate scope. All structural components of the catalyst cooperatively participate in the stereocontrolling event.

Nature harnesses weak interactions, particularly hydrogen bonds, to construct biologically active supramolecular architectures, as demonstrated by the three-dimensional structures of enzymes and nucleic acids. Inspired by these biological systems, research for the development and application of supramolecular catalysts assembled through noncovalent interactions has attracted interest in the fields of both selective chemical synthesis and molecular recognition (*1*). Despite important advances in the elaboration of self-assembled molecular receptors and catalyst systems, however, rational design of chiral supramolecular catalysts for stereoselective bond-forming reactions by the use

Department of Applied Chemistry, Graduate School of Engineering, Nagoya University, Nagoya 464-8603, Japan.

*To whom correspondence should be addressed. E-mail: tooi@apchem.nagoya-u.ac.jp